Seismic resonances of spherical acoustic cavities

F. M. Schneider[1*], S. Esterhazy[1,2],

I. Perugia[2], G. Bokelmann[1]

[1] Department of Meteorology and Geophysics, University of Vienna, Austria

[2] Faculty of Mathematics, University of Vienna, Austria

March 6, 2017

*Corresponding author: felix.schneider@univie.ac.at

This article has been accepted for publication and undergone full peer review but has not been through the copyediting, typesetting, pagination and proofreading process, which may lead to differences between this version and the Version of Record. Please cite this article as doi: 10.1111/1365-2478.12523.

Abstract

We study the interaction of a seismic wave-field with a spherical acoustic gas- or fluid-filled cavity. The intention of this study is to clarify whether seismic resonances can be expected, a characteristic feature, which may help detecting cavities in the subsurface. This is important for many applications, as in particular the detection of underground nuclear explosions which are to be prohibited by the Comprehensive-Test-Ban-Treaty. In order to calculate the full seismic wave-field from an incident plane wave that interacts with the cavity, we considered an analytic formulation of the problem. The wave-field interaction consists of elastic scattering and the wave-field interaction between the acoustic and elastic media. Acoustic resonant modes, caused by internal reflections in the acoustic cavity, show up as spectral peaks in the frequency domain. The resonant peaks coincide with the eigenfrequencies of the undamped system described by the particular acoustic medium bounded in a sphere with stiff walls. The filling of the cavity could thus be determined by the observation of spectral peaks from acoustic resonances. By energy transmission from the internal oscillations back into the elastic domain, the oscillations experience damping, resulting in a frequency shift and a limitation of the resonance amplitudes. In case of a gas-filled cavity the impedance contrast is still high, which means low damping of the internal oscillations resulting in very narrow resonances of high amplitude. In synthetic seismograms calculated in the surrounding elastic domain, the acoustic resonances of gas-filled cavities show up as persisting oscillations. However, due to the weak acoustic-elastic coupling in this case the amplitudes of the oscillations are very low. Due to a lower impedance contrast, a fluid-filled cavity has a stronger acoustic-elastic coupling, which results in wide spectral peaks of lower amplitudes. In the synthetic seismograms derived in the surrounding medium of fluid-filled cavities, acoustic resonances show up as strong but fast decaying reverberations.

KEYWORDS: CAVITY DETECTION, SEISMIC WAVE MODELING , ELASTO-ACOUSTIC COUPLING, RESONANCE SEISMOMETRY, CTBTO

Introduction

Investigation and detection of underground cavities is a challenge that is an essential ingredient for the realization of the Comprehensive Test Ban Treaty (CTBT), which aims to prohibit any nuclear explosion on earth including underground nuclear explosions (UNEs). Verification of possible violations of the treaty requires techniques to detect remnants of UNEs as in particular the cavity created by melting and compression of the surrounding material. In case a suspicious seismic event is detected by the International Monitoring System (IMS) operated by the Comprehensive-Test-Ban-Treaty- Organization (CTBTO), each member state can request an On-Site Inspection (OSI) at the location of the event. During such an OSI, a field team delegated by the CTBTO uses several techniques to verify whether an UNE has been conducted at the particular site. Beside aftershocks, radioactive vestiges and suspicious infrastructure, the location and detection of the cavity is a major target during an OSI (Adushkin and Spivak, 2004). As seismic technique for cavity detection, the CTBT lists "Resonance Seismometry", for which a proper definition is still missing and which this work is dedicated to. However, the detection of cavities in the subsurface is important in many other aspects as for example for the evaluations of the geohazard potential of a region that might suffer sinkhole activity (Krawczyk et al., 2012). Unlike other applications as detection of former mines or voids from salt dissolution, only small gravimetric anomalies are expected in case of a cavity created by UNEs since no material is lost but only compressed and distributed around the cavity. Moreover, for UNEs that are not directly visible at the surface, the depth of the cavity is too deep to be registered by ground penetrating radar (Houser, 1970). Electromagnetic methods however could also be used to complement the observations of a seismic survey.

In order to compute the interaction of the seismic wave-field with the acoustic cavity, we use an analytic approach (Korneev and Johnson, 1993). Similar analytic description had been also derived before by Hinders (1991) and re-derived by Ávila-Carrera and Sánchez-Sesma (2006). Gritto (2003) invented a scheme using Korneev's approach for void detection using seismic tomography. Tomographic approaches and seismic reflection from shear wave sources have been used successfully to detect tunnels and voids close to the surface (Sloan et al., 2015; Krawczyk et al., 2012). Spatial spectrograms can be used for the detection of low velocity inclusions as increase of certain spectral peaks (Lambert et al., 2011).

Korneev (2009) showed that resonances from circumferential waves can be observed for fluid-filled cavities. In this paper we focus on acoustic resonances that appear during interaction of the seismic wave-field with the cavity which could be utilized for a cavity-detection technique. Using an exact analytical solution of the problem, we demonstrate the occurrence of resonance-peaks and relate their appearance to the acoustic eigenmodes of the cavity. We show that the resonance peaks in the frequency-domain translate to internal acoustic reverberations in the time-domain. Furthermore the influence of intrinsic attenuation is studied by using a visco-acoustic elastic formulation. The analytical approach that we implemented is sketched in the next section. For further reading and deeper understanding we also refer to Korneev and Johnson (1996), where the derivation is presented in a more detailed way.

Analytical Approach

In order to calculate the seismic wave-field in and around a cavity that is exposed to a plane or spherical seismic wave, we follow the derivation by Korneev and Johnson (1993). In this approach, the vector-valued displacement field is divided in the incident field $\tilde{\mathbf{u}}_{\mathbf{0}}$ and the secondary fields $\tilde{\mathbf{u}}_{\mathbf{1}}$, which represents the displacement field inside the cavity and $\tilde{\mathbf{u}}_{\mathbf{2}}$, the scattered field in the outer domain, see Fig. 1. In the outer domain, the total displacement field is given by $\tilde{\mathbf{u}}_{\mathbf{0}} + \tilde{\mathbf{u}}_{\mathbf{2}}$. All displacement fields are assumed to be harmonic in time:

$$\tilde{\mathbf{u}}_{\nu}(\mathbf{r}, t) = \mathbf{u}_{\nu}(\mathbf{r})\mathrm{e}^{i\omega t}, \tag{1}$$

where $\omega = 2\pi f$ is the angular frequency. Therefore only the spatial problem is solved for individual frequencies.

Throughout this paper, a plane P-wave is considered as incident field, however the formulation of Korneev and Johnson (1996) also allows for spherical incident waves and shear waves. The three fields are related to each other at the interface of the cavity by certain transmission conditions. These transmission conditions take into account the continuity of displacements amplitudes as well as the continuity of the traction vector on the sphere defined by the cavity interface. For the case of an acoustic medium inside the cavity, only the normal components need to be considered:

$$\mathbf{u}_{\mathbf{1}} \cdot \mathbf{n} = (\mathbf{u}_{\mathbf{0}} + \mathbf{u}_{\mathbf{2}}) \cdot \mathbf{n} \tag{2}$$

$$\mathbf{t}(\mathbf{u}_{\mathbf{1}}) \cdot \mathbf{n} = \mathbf{t}(\mathbf{u}_{\mathbf{0}} + \mathbf{u}_{\mathbf{2}}) \cdot \mathbf{n}, \tag{3}$$

where the traction vector $\mathbf{t}$ on the spherical surface with unit radius $\hat{\mathbf{r}}$ and the Lamé parameters λ and μ is given by

$$\mathbf{t}(\mathbf{u}) = \lambda \nabla \cdot \mathbf{u}\, \hat{\mathbf{r}} + 2\mu \frac{\partial \mathbf{u}}{\partial r} + \mu[\hat{\mathbf{r}} \times \nabla \times \mathbf{u}]. \tag{4}$$

General formulations of the three displacement fields are derived by making use of the spherical symmetry of the setting and expanding the three displacement fields in terms of spherical harmonic vectors $\mathbf{Y}^{+,-}_{\mathbf{lm}}$.

The representation of a plane incident P-wave directing along the positive z-axis in terms of spherical harmonic vectors is:

$$\begin{aligned}\mathbf{u_0} &= \mathrm{e}^{ik_p z}\hat{\mathbf{z}} \\ &= \sum_{l\leq 0}\left(j_{l+1}(k_p r)\mathbf{Y}^{+}_{\mathbf{l0}} - j_{l-1}(k_p r)\mathbf{Y}^{-}_{\mathbf{l0}}\right)\exp(-\frac{i\pi(l+1)}{2}),\end{aligned} \tag{5}$$

where $k_p = (2\pi f)/v_p$ is the wave number of the P-wave and $\hat{\mathbf{z}}$ is the unit vector in z-direction. Korneev and Johnson (1996) show that the secondary displacement fields inside and outside the spherical cavity can generally be written in the form

$$\begin{aligned}\mathbf{u_1} = \sum_{l\leq 0}\Bigg(&\Big(\ a_l^{(1)} j_{l+1}(k_{p,1}r) + l\ b_l^{(1)} j_{l+1}(k_{s,1}r)\Big)\mathbf{Y}^{+}_{\mathbf{l0}} \\ &+\Big(-a_l^{(1)} j_{l-1}(k_{p,1}r) + (l+1)\ b_l^{(1)} j_{l-1}(k_{s,1}r)\Big)\mathbf{Y}^{-}_{\mathbf{l0}}\Bigg)\exp(-\frac{i\pi(l+1)}{2})\end{aligned} \tag{6}$$

and

$$\begin{aligned}\mathbf{u_2} = \sum_{l\leq 0}\Bigg(&\Big(\ a_l^{(2)} h_{l+1}(k_{p,2}r) + l\ b_l^{(2)} h_{l+1}(k_{s,2}r)\Big)\mathbf{Y}^{+}_{\mathbf{l0}} \\ &+\Big(-a_l^{(2)} h_{l-1}(k_{p,2}r) + (l+1)\ b_l^{(2)} h_{l-1}(k_{s,2}r)\Big)\mathbf{Y}^{-}_{\mathbf{l0}}\Bigg)\exp(-\frac{i\pi(l+1)}{2}).\end{aligned} \tag{7}$$

Here, $k_{p/s,1}$ and $k_{p/s,2}$ are the wave numbers of P/S-waves inside and outside of the cavity, respectively. The spherical Bessel functions (j_l) and spherical Hankel functions of the second kind (h_l) are regular at the origin and satisfy the radiation condition at large distances, respectively. In this way the solution of the problem is reduced to finding the right scalar coefficients a_l^ν and b_l^ν, which are determined by imposing the transmission conditions at the acoustic-elastic interface, given in Eqs. 2 and 3. This yields a set of linear equations for each l which can be solved iteratively. Analytic expressions for a_l^ν and b_l^ν depending on frequency and the model parameters density, compressional and shear velocities (ρ, v_p and v_s) of the elastic and acoustic domains are given in the Appendix of Korneev and Johnson (1993).

Acoustic resonances

Appearance of resonant peaks

The appearance of acoustic resonances inside the cavity are studied for the cases of a gas-filled and a fluid-filled cavity in an elastic surrounding. The parameters chosen for the study are listed in Table 1. For the size of the cavity a radius of 30 m is chosen. The scattering regime, defined by the ratio of the circumference and the wave length

$$\frac{U}{\lambda} = \frac{U}{v_p}f = \frac{2\pi R}{v_p}f, \tag{8}$$

depends on the frequency f of the incidence wave. For our choice of elastic parameters the factor $\frac{2\pi R}{v_p}$ is approximately 0.05 s, i.e. our simulations are in the regime of Rayleigh scattering for frequencies $f < 20$ Hz ($U/\lambda < 1$), in the regime of Mie scattering for $f \approx 20$ Hz ($U/\lambda \approx 1$) and in the regime of geometrical scattering for $f > 20$ Hz ($U/\lambda > 1$).

Using the analytic approach described in the previous section, the amplitude spectra of the scattered wave-field from an incident P-wave are derived at the locations depicted in Fig. 2 inside and outside of the cavity for different acoustic parameters, representing different fillings of the cavity. Fig. 3 shows the amplitude spectrum of the scattered field outside the cavity (positions depicted as red dots in Fig. 2) if the cavity is empty, i.e. the density of the acoustic medium is zero which is referred to as the case of a vacuum inclusion. The spectra of the vacuum inclusion are smooth functions that are monotonously increasing for small frequencies. In the transmitted wave-field ($\theta = 0$) the spectrum shows long-period modulations. We consider $v_p = 4000$ m/s as a reference value. Amplitude spectra for $v_p = 3000$ m/s and $v_p = 5000$ m/s (and v_p/v_s=1.73), depicted in dashed lines, show that the velocity of the outer medium controls the frequency of the modulations. For the other scattering angles ($\theta > 0$) the spectra are also stretched or squeezed for faster and lower velocity of the elastic medium, respectively.

Amplitude spectra of the cavity filled with an acoustic medium are calculated inside and outside of the cavity at the locations shown as blue and red dots in Fig. 2. The upper and lower halfs of each panel in Figs. 4 and 5 show the corresponding spectra inside and outside the gas- and fluid-filled cavity.

In the gas-filled case (Fig. 4), the spectra from the outer domain behave similar to the spectra from the vacuum inclusion (depicted with dashed green lines) with the difference that sharp resonance peaks are present on top of the spectral variation of the vacuum inclusion. Peaks occur for both domains inside and outside the cavity at the same frequencies. However, the amplitudes of the peaks inside the cavity have five orders of magnitude higher values than those outside the cavity. These high amplitudes of the inner oscillations and the co-appearance of the spectral peaks at the same frequencies suggest that excitation of resonant modes in the acoustic domain is responsible for the spectral peaks also in the elastic domain.

For the fluid-filled cavity (Fig. 5), the spectra from the outer domain also follow the spectra from the vacuum inclusion, but the deviations from the case of the vacuum inclusion form broader peaks of lower amplitudes compared to the case of a gas-filled cavity. The spectra inside the fluid-filled cavity also show broad resonances coinciding with the deviations from the case of vacuum inclusion in the outer domain. For the fluid-filled cavity, the amplitudes of the resonant peaks inside and outside the cavity are comparable in size.

Eigenfrequencies of the acoustic cavity

To approximate the resonant frequencies of the acoustic-elastic system, the eigenfrequencies of an acoustic cavity with stiff boundaries are derived for the case of boundaries that do not move at all. Therefore the displacement field has to become zero at the boundary of the cavity. This is expressed mathematically by Dirichlet boundary conditions. However, in the purely acoustic domain, it is easier to consider the scalar pressure field instead of the 3D displacement field. The 3D-displacement field can be derived from the scalar pressure field $\tilde{P}(\mathbf{r},t)$ by Newton's law

$$\nabla \tilde{P}(\mathbf{r},t) = -\rho \frac{\partial^2}{\partial t^2} \tilde{\mathbf{u}}(\mathbf{r},\mathbf{t}), \tag{9}$$

which turns in the considered time-harmonic case into

$$\mathbf{u} = \frac{1}{\rho\omega^2} \nabla P. \tag{10}$$

Hence, the eigenfrequencies of the pressure and displacement fields are identical. For the pressure, Neumann boundary conditions have to be considered for the case of stiff walls. The eigenvalues are derived by applying a product ansatz $P = R(r)Y(\theta,\phi)$, that separates radial and angular components, to the scalar Helmholtz equation

$$\Delta P + k^2 P = 0, \quad k = \omega / v_p. \tag{11}$$

The solutions of the radial part are

$$R(r) = j_l(kr), \tag{12}$$

where j_l are the spherical Bessel functions (see for example Budak et al. (1988) or Grebenkov and Nguyen (2013)). For Neumann boundary conditions, the first derivative $j_l'(kr)$ has to become zero at $r = R$, which lead to the eigenfrequencies

$$f_{nm} = \frac{j_{nm}' \, v_p}{2\,\pi\,R}, \tag{13}$$

where j_{nm}' are the m-th root of the derivative of the n-th spherical Bessel function. For the displacement, the first derivatives of the spherical Bessel functions $j_n'(k_{nm}r)$ describe the radial part of the eigenmodes, when $k_{nm} = 2\pi f_{nm}/v_p$. The roots j_{nm}' have been derived numerically for spherical Bessel functions of order zero to five. The vertical bars in the lowermost panels in Fig. 4 and Fig. 5 show the eigenfrequencies substituting the corresponding parameter values ($R = 30$ m and $v_p = 300$ m/s or $v_p = 1400$ m/s for the gas- or fluid-filled cases) in Eq. 13. For each order of the spherical Bessel function there exist a discrete set of eigenvalues. To distinguish the order of the Bessel function, each set of the corresponding eigenvalues is displayed with a different height as noted at the y-axis. For both the gas-filled and the fluid-filled cavity, the eigenfrequencies coincide with the spectral peaks derived from the calculation of the full wave-field. While for the gas-filled case the match seems to be very close, in the fluid-filled case the resonant frequencies of the acoustic-elastic system appear to be shifted to lower frequencies.

Nature of resonances

In Fig. 6, the appearance of acoustic resonances is illustrated by the example of the eigenmode j_{04}. The computation has been derived for the gas-filled cavity at the eigenfrequency $f_{res} = 22.387$ Hz. We computed the full wave-field for an incident P-wave with frequencies f_{res} as well as slightly below and above it. Only the incident fields for slightly larger and smaller frequencies than the resonance frequency ($f = 22.0$ Hz and $f = 22.5$ Hz) are displayed here. The scattered fields in the elastic domain for frequencies larger and smaller than the eigenfrequency are similar to each other. Even if the pattern inside the cavity changes, no effect is visible in the outer domain where the scattered field is dominated by the reflected incident field. At the eigenfrequency of the cavity, the scattered field shows strong deviations from the scattered field for $f = 22.0$ Hz and $f = 22.5$ Hz. Inside the cavity an eigenmode is excited leading to the target pattern of the radial component with large amplitudes. Fig. 6 d shows a zoom into the cavity for the excited resonant mode. As expected for the Neumann-mode j_{04}, the radial component of the displacement coincides with the derivative of the Bessel function j_0', which has four zeros for $30 \geq r > 0$, corresponding to four antinodes between the center and the boundary of the cavity. At the eigenfrequency, in addition to the reflection of the incident field, transmitted energy from the cavity back in the outer domain provide a significant part of the scattered field. In the total fields, which are displayed in the right column of Fig. 6, an effect of the resonance is visible also in the elastic domain. While for $f = 22.0$ Hz and $f = 22.5$ Hz the total fields in the outer domain are similar to each other, in case of the excited eigenmode some part of the incident field is suppressed above the cavity.

To study the dependency of the resonance peaks from the impedance contrast between the acoustic medium inside the cavity and the elastic surrounding medium, the effect of changing density of the acoustic medium on the resonance peaks is investigated. By changing the density, the impedance $Z = \rho v_p$ of the acoustic medium is changed without affecting the eigenfrequency of the acoustic cavity, since the eigenfrequency is determined by the radius (R) and the velocity (v_p) of the medium only (see Eq. 13). As examples, in the following, the resonance peaks at eigenmodes j_{04} and j_{13} are shown to demonstrate the effect of a changing impedance contrast for a gas- and fluid-filled cavity, respectively.

Gas-filled cavity

Fig. 7 shows the resonant peak for Neumann mode j_{04} at 22.387 Hz, for different densities of the acoustic medium, inside (a) and outside (b) of the cavity. The velocity of the acoustic medium is fixed to 300 m/s, which is the acoustic velocity in gas. The amplitude resonant peak inside the cavity shows strong dependency on the impedance contrast. The resonant peak has the highest amplitude for $\rho = 1$ kg/m^3, which corresponds to the gas-filled case. Duplication of the density of the acoustic medium yields bisection of the maximum amplitude of the resonant peak. At the same time, the resonant frequency shifts to smaller values. This dependency of amplitude reduction and frequency shift of the resonance peak on increasing impedance resembles the behavior of a damped driven oscillator for increasing damping. In the outer medium (see Fig. 7b) the maximum amplitude of the resonance peak is not affected, however the frequency shift to lower frequencies of the maximum amplitude is also observed as well as a broadening of the resonance peak. For the gas-filled case ($\rho = 1$ kg/m^3), the resonant peak is the closest to the eigenfrequency of the acoustic medium (depicted by the black dashed line) and shows the narrowest width.

In Fig. 8a, the phase difference of the complex displacement field inside and outside the cavity is shown. As expected for a damped driven oscillator, the value of the phase-difference performs a shift of 2π at the resonance frequency. As in case of increasing damping of the damped driven oscillator, the phase shift becomes smoother for increasing density, which corresponds to a decreasing impedance contrast between cavity and surrounding medium.

Fluid-filled cavity

The spectra in Fig. 4 and Fig. 5 show that for the case of a fluid-filled cavity the resonance peaks are less sharp and much lower in amplitude than in case of a gas-filled cavity. As an example, the resonant peak for the fluid-filled cavity close to the Neumann mode j_{13} is investigated. The seismic velocity of the fluid is fixed to 1400 m/s and the impedance contrast is varied by changing the density of the acoustic medium. The fluid-filled case corresponds to the density $\rho =$ 1024 kg/m^3. Fig. 8b shows the phase difference of the complex displacement field inside and outside the cavity. While for higher impedance contrast ($\rho = 128$ kg/m^3) a phase shift at the eigenfrequency is present similar to the phase shift of gas-filled cavity shown in Fig. 8a, for increasing densities the phase shift becomes less apparent. The amplitude peaks inside and outside the cavity are shown in Figs. 9 a) and b), respectively. As in case of the gas-filled cavity, the peak amplitude inside of the cavity is strongly affected by variation of the density. The peak prominence is decreasing for increasing densities, while the width increases. In the elastic domain the amplitude is less affected, but decreases for increasing density. As in the gas-filled case, the width of the resonance peak is increasing for increasing density.

Compared to the gas-filled case, in the case of a fluid-filled cavity the energy transmission from the acoustic cavity into the elastic domain is higher causing higher damping of the internal oscillations. The vanishing phase shift and shrinking peak prominence for higher values of ρ suggest that the system is close to the over-damped case, where resonances naturally vanish.

Wave-field along seismic profile

To mimic an experimental setup for a field campaign, we computed the seismic wave-fields for a profile 250 m above the cavity for a plane incident wave from below. The geometry is shown in Fig. 10. Note that no free-surface is included in the model, however the spectral characteristics of the wave-field-cavity interaction should not be affected. The parameters chosen for the gas-filled and fluid-filled cavity and the outer elastic medium are again those listed in Table 1.

Spatial spectrograms

The amplitude spectra of the scattered fields along the profile are shown in Fig. 11 as spatial spectrograms. Figs. 11 a) and b) show the spatial spectrograms for the gas-filled and fluid-filled cavity, respectively. The long period variations, which are determined by the geometry of the cavity and the velocity of the surrounding medium, in both cases look very similar. These long period variations vary with the distance from the cavity. This pattern is overprinted with the resonance frequencies of the cavity, which are independent of the distance and therefore show up as vertical lines in the spatial spectrograms. In Figs. 11 c) and d), the long period variations are filtered out by applying a high-pass filter to the spectrum. In this way the long amplitude variations from the external scattering of the cavity are suppressed and the resonance frequencies are enhanced. In Fig. 11 c), for the gas-filled cavity a zoom into the frequency range $0-32.14$ Hz is shown. Since the eigenmodes depend on the acoustic velocity, the gas-filled cavity shows in this range the same eigenmodes as the fluid-filled cavity in the range $0-150$ Hz, shown in Fig. 11 d). Note that the resonant peaks are slightly shifted with respect to the Neumann-modes, depicted as dashed lines, which is apparent only in the fluid-filled case.

Synthetic seismograms

From the time-harmonic solutions derived for individual frequencies, synthetic seismograms are computed by inverse discrete Fourier transformation. Time-harmonic solutions corresponding to frequencies ranging from 0.1 Hz to 200 Hz with intervals $\Delta\ f$ of 0.1 Hz were superimposed and a Gaussian taper function of the form

$$g(\omega) = \mathrm{e}^{-\left(\frac{\omega}{2\pi a}\right)^2} \tag{14}$$

with $a = 100$ Hz was applied in order to generate a Gaussian pulse as incident field. This yields synthetic seismograms

$$\mathbf{s}_\nu(\mathbf{r}, t) = \mathrm{Re}\left(\sum_\omega \mathbf{u}_{\omega,\nu}(\mathbf{r})\ g(\omega)\ \mathrm{e}^{i\omega t}\right), \tag{15}$$

where $\nu = 0$ and $\nu = 2$ corresponds to seismograms for the incident and scattered field, respectively. Seismograms for the total field are computed by summation of incident and scattered wave-field seismograms $\mathbf{s_0(t)}$ and $\mathbf{s_2(t)}$.

We computed synthetic seismograms for all locations along the profile (Fig. 10). Traces of Fig. 12 represent synthetic seismograms for the gas-filled cavity. The vertical aligned arrival at 0.065 s in Fig. 12a represents the incident plane P-wave pulse, which is only visible on the vertical component of the total field. The later arrivals are a reflected P-wave followed by a P-to-S converted wave scattered at the cavity. On the horizontal component of the total field displayed in Fig. 12b, only scattered waves are present since the incident wave consist only of vertical particle motion. Fig. 12c and Fig. 12d show only seismograms from the scattered wave-field $\mathbf{u_2}$. Here the synthetic seismograms are rotated with respect to the cavities center in order to separate scattered P- and S-energy on L- and Q-component, respectively (orientation of L and Q depicted in Fig. 10). In Fig. 12a and Fig. 12b two v-shaped arrivals are present, the earlier one from the scattered P- and the later one the scattered S-energy. On the L-component in Fig. 12c only the earlier v-shaped phase from the scattered P-energy is present which is suppressed on the Q-component, shown in Fig. 12d. Note that, since the scatterer is not just a point, separation of P-and S-energy works not perfectly for low distances from the cavity.

Fig. 13 shows the same scenario as Fig. 12 for a fluid-filled cavity. Since the outer medium is the same, incident wave and primary scattered waves behave very similarly to the case of the gas-filled cavity. However, multiple reverberations that show up as later arrivals of the primary scattered waves are present. On the L- and Q-component in Fig. 13c and Fig. 13d, it is apparent that P-and S-waves originate from the cavity, since in each figure later v-shaped arrivals could be isolated from waves that travel with P- and S-velocities, respectively. Thus, the cavity becomes a secondary source of a damped oscillating signals. In the next section we show that these signals originate from energy trapped in internal oscillations in the acoustic medium.

The presented computations in this section have been done for the transmission regime. Computations for the back-scattered regime show equivalent results in terms of appearance of resonances. For comparison, the results are shown in the Appendix.

Internal reflections as cause of acoustic resonances

In this section we investigate the transition from a fluid-filled cavity with strong visible reverberations to the gas-filled cavity, where the synthetic seismograms show only signals from the primary scattered waves. To study the influence of velocity and density, multiple synthetic seismograms for changing parameters are derived. Each parameter is varied individually starting with the parameter set of a fluid-filled cavity. Firstly, only the velocity of the acoustic medium is reduced without changing its density (Fig. 14). In Fig. 15 the 3D-wave-field for an impulsive source is investigated on a 2D-section through the cavity in order to get an insight into the dynamics of the interacting wave-fields. In a later step, the density is decreased without changing the acoustic velocity (Fig. 16 and 17).

The upper row in Fig. 14 shows a synthetic seismogram of the back-scattered field ($\phi = \pi$) outside of the cavity for the fluid-filled cavity ($v_1 = 1400$ m/s, $\rho_1 = 1024$ kg/m^3). On the left, a zoom into the first 0.4 s that contains the primary scattered wave for $t < 0.27$ s is shown. On the right, a time series of 6 s is displayed. For $v_1 = 1400$ m/s, strong later arrivals follow the primary scattered wave at $t = 0.28$ s that is damped out fast. Decreasing v_1 yields a shift of the later arrivals to longer times. Lines 2-5 of Fig. 14 show similar synthetic seismograms as in the first line with successively decreased velocity of the acoustic medium. The primary scattered pulse ($t < 0.27$ s) remains for all lines the same while the signal from the later arrivals are stretched, they become initially smaller in amplitude but more persistent over time.

For the parameter set of the lowest panel in Fig. 14 ($v_1 = 300$ m/s and $\rho_1 = 1024$ kg/m^3), the full wave-field for a linear source pulse is computed by deriving synthetic seismograms on a 2D-grid through the cavity. To derive 2D-sections we computed synthetic seismograms, as described in the previous section, at about 40000 locations on a vertically oriented 400 m $\times$ 400 m grid with a grid spacing of 2 m. Snap-shots of the generated movie are displayed in Fig. 15, where the z-component of the total field is displayed color-coded for a sequence of nine points in time between $t = 0.2$ s (Fig. 15a) and t= 0.625 s (Fig. 15i). In Figs. 15a and 15b the incident linear impulsive source is passing the cavity and the primary scattered wave-field is generated. Moreover a field is induced into the cavity describing an up and down bouncing wave. Firstly it is propagating upwards (Figs. 15c - 15d). Then a part of the induced acoustic field from within the cavity couples out back into the elastic domain starting at $t \approx 0.3975$ s mainly towards the upper hemisphere (Figs. 15e - 15f). The remaining part of the upgoing wave is reflected at the upper wall of the cavity resulting in a downward propagation (Fig. 15g). At $t \approx 0.6$ s (Figs. 15h - 15i) a part of the acoustic field couples out again in the elastic domain, this time mainly towards the lower hemisphere. Hence the later arrivals in Fig. 14 are caused by internal reverberations of the acoustic medium coupling out into the elastic domain again. For decreasing v_1, the internal reflections need more time to cross the cavity which causes the stretching of the pattern. Further, the impedance contrast increases for decreasing v_1 which causes a decrease of the transmission coefficient and hence the damping of the internal oscillations to decay. This explains the longer persistence of the later arrivals.

As the lowest line of Fig. 14, the uppermost line of Fig. 16 shows again synthetic seismograms of the scattered field for the parameter set used for the computation of the snapshots in Fig. 15. Here the internal reflections show up as repeating signals with $\approx 1/10$ amplitude of the primary scattered wave. The 2nd to 5th lines show the transition to the gas-filled cavity by decreasing the density of the acoustic medium successively to 1 kg/m^3, which corresponds to the gas-filled case. The left column show that the primary scattered wave is not strongly affected by changing the density of the acoustic medium. The later arrivals, caused by internal reflections does not change their internal distances, whereas their amplitudes become smaller and are not visible anymore in the gas-filled case.

Zooming into the traces, as shown in Fig. 17, however shows, that the peaks from internal reflections are present also for lower densities. On the one hand, for lower densities the amplitudes become smaller, but on the other hand also the decay of the oscillations becomes slower. Thus, the signals become more persistent in time, which can again be explained by the lower damping of the internal oscillations due to the decreasing energy transmission for an increasing impedance contrast.

Effect of intrinsic attenuation for gas-filled cavities

So far no intrinsic attenuation has been considered in the modeling. Mathematically, this is expressed by the imaginary parts of the Lamé parameters λ and μ being zero. Acoustic attenuation in gas and water are very small, which is why it can be neglected in most applications. In the case of resonances however a small attenuation can have a large effect. Without considering internal attenuation the damping of the waves inside the cavity is only given by the energy transmission through the interface. In case of a gas-filled cavity the impedance contrast at the interface is very high resulting in a low energy loss from the acoustic into the elastic medium. In this section the effect of intrinsic attenuation in the acoustic medium is studied for the gas-filled cavity, since for this case, attenuation can account for a significant part of the damping of internal oscillation. Since in any case $\mu = 0$ in the acoustic domain, only the effect of a non-zero imaginary part of λ is investigated.

The attenuation of acoustic waves in air, namely $\mathrm{Im}(\lambda)$, is frequency-dependent. We used the attenuation values for air at the surface, given as attenuation coefficient α by Sutherland and Bass (2006), and transferred them to values of the seismic Q-factor, defined as

$$Q = \frac{\mathrm{Re}(\lambda)}{\mathrm{Im}(\lambda)}. \tag{16}$$

The conversion from α to the Q-factor is given by (Carcione, 2014)

$$Q = \frac{\pi f}{v_p \alpha}. \tag{17}$$

The resulting Q-values are given in Fig. 18. The discrete values for Q are fitted by the function $Q(f) = a/f$ with $a = 64.1$ kHz, which we used to compute Q-values for each frequency.

The intrinsic attenuation is implemented in the analytical solution by taking into account complex velocities. For vanishing shear modulus, real and imaginary parts of λ can be expressed as

$$\mathrm{Re}\,\lambda = v_p^2\,\rho \tag{18}$$

and, by definition of Q in Eq. 16,

$$\operatorname{Im}\lambda = \frac{\operatorname{Re}\lambda}{Q} = \frac{v_p^2\,\rho}{Q}, \tag{19}$$

which yields for the complex p-velocity c_p of the attenuated acoustic medium

$$c_p = \sqrt{\frac{\lambda}{\rho}} = v_p\sqrt{1+\frac{i}{Q}}, \tag{20}$$

where v_p is the p-velocity of the unattenuated medium.

The effect of intrinsic attenuation is displayed in Figs. 19 and 20. Fig. 19 compares the unattenuated case to the case considering intrinsic attenuation. In Figs. 19a and 19b, the spectral amplitudes of the total field are shown for the back-scattering domain ($\theta = 180°$) and Figs. 19c and 19d show the corresponding seismograms derived by inverse Fourier transform, for the unattenuated and the attenuated case, respectively. In the seismograms a zoom factor is chosen to display the internal reflections corresponding to the acoustic resonances. The acoustic resonances, showing up as sharp peaks in the spectrum, are strongly decreased for the attenuated case. Due to the frequency dependence of Q (see Fig. 18) larger frequencies are more strongly affected by the attenuation and the resonance peaks are hardly visible for $f > 20$ Hz. In the corresponding seismograms, however, the differences are not very strong in the first 30 s. The attenuation of the internal oscillations becomes evident after roughly 10 s.

In practical applications the size of the resonance peaks also depends on the length of the time window that is involved in the measurement. Since the oscillation is decaying faster for the attenuated case the effect of attenuation in the spectrum is larger for longer time windows. To demonstrate this we recalculated the spectrum from the synthetic seismograms taking into account a short time window (30 s) and a long time window (1h) and compare the attenuated and the unattenuated cases. To expose the resonance peaks a high pass (HP) filter is applied to the spectrum. For the HP-filtered spectrum $A_{HP}(f)$, the spectrum $A(f)$ is filtered by

$$A_{HP}(f) = \mathscr{F}^{-1}(\mathscr{F}(|A(f)|)\,T(t)), \tag{21}$$

where $\mathscr{F}$ is the Fourier transform and $T(t)$ is a taper function obeying $T(t) = 0$ for $|t| < 0.5$ s, $T(t) = 1$ for $|t| > 0.5$ s, and T(t) having with a smooth transition from 0 to 1 for $0.5\text{ s} < |t| < 1.5$ s. The spectrum and the HP-filtered spectrum for the short time window (30 s) are shown in Figs. 20a and 20b, the corresponding spectra for the long time window (1h) is displayed in Figs. 20c and 20d. For the short time window the absolute size of the resonant peaks is small. Thus, the resonant peaks are only visible in the HP-filtered version of the spectrum (Fig. 20b). In this figure the difference of the attenuated (green solid line) and unattenuated case (thin black dashed line) is small. For the long time window the spectral peaks become larger and are also visible in the direct spectrum (Fig. 20c). In the HP-filtered version (Fig. 20d) the difference of the

attenuated and the unattenuated case become clearly evident. Resonance peaks are decreased and the difference is increasing for larger frequencies.
From this investigation it can be concluded that attenuation can not be neglected for the case of acoustic resonances in a gas-filled cavity. For realistic attenuation parameters the observation of resonance peaks in the gas-filled cavity can be expected mainly at low frequencies and can be emphasized by using additional high-pass filter in the spectral domain.

Implications and Outlook

The described results yield some possible diagnostics for cavity detection, which is needed for nuclear verification. As remnants from underground nuclear tests, the cavity is a major structural feature that is to be found by nuclear inspectors during On-Site Inspections. The presence of acoustic resonances can in principle be detected rapidly through spatial spectrograms as shown in Fig. 11. As possible diagnostic tools, either the direct scattered energy from a cavity could be used, which shows long period variations in frequency and an increased intensity above the cavity (Figs. 11a and 11b), or spectral peaks from acoustic resonances could be extracted (Figs. 11c and 11d). The next step is to use this knowledge and apply it to more sophisticated numerical simulations and/or real data in order to verify whether acoustic resonances can be resolved in a realistic setting. In the presented analytical study, some model simplifications have been considered. First, the geometry of the cavity is described by a perfect sphere. In real-live situations acoustic resonances could be weakened by defocusing effects. Second, the filling of the cavity is assumed to be homogeneous and purely acoustic. However, in real cavities from underground nuclear explosions, a rubble zone is present in and around the cavity. Third, all media are assumed to be isotropic and, fourth, no free surface is present in the presented geometry, i. e. the interaction with surface waves is neglected, which could complicate the observation. All these issues will be addressed by further studies using e.g. finite-element-modeling that can handle more complex geometry and experimental studies of analogue sites. For example, as an analogue for a cavity from a nuclear explosions, the CTBTO has selected a natural cavity in northern Hungary (Felsőpéteny). At this site, active seismic surveys have been conducted between 2012 and 2014 (Tóth et al., 2015) that are now planned to be inspected in the light of our theoretical findings presented in this paper.

Conclusions

Acoustic resonances are present in case of a gas-filled and in case of a fluid-filled cavity causing a significant change of the transfer function of the ground compared to the case of a vacuum cavity. In the vicinity of a resonant frequency, the acoustic cavity exposed to a seismic wave-field shows a behavior similar to that of a damped driven oscillator: the seismic wave-field acts as driving force and the energy transmission from the acoustic back into the elastic domain acts as damping of the internal oscillations. In case of no intrinsic attenuation, the damping is therefore defined by the inverse of the impedance contrast between the acoustic and the elastic domain.

In case of a gas-filled cavity, the impedance contrast between elastic and acoustic medium is high, which cause low amounts of energy to be transmitted from the acoustic medium back into the elastic domain. Internal oscillations are therefore nearly undamped and resonance occurs in very narrow frequency ranges, which are very close to the eigenfrequencies of the acoustic cavity bounded by stiff non-elastic walls. If the impedance contrast is reduced slightly, the damping of the internal oscillations increases in the same amount as the energy-transmission to the outer medium increases. Higher damped internal resonance peaks, which are lower in amplitude but broader in frequency range, cause therefore broader resonance peaks in the elastic domain that have the same peak amplitudes as in the case of unreduced impedance contrast. This argumentation holds as long as the damping of the internal oscillations is small and far below critical damping where the oscillations become overdamped and the resonances disappear. Due to the low damping by means of energy transmission rate in the case of gas-filled cavities, intrinsic attenuation of acoustic waves has a significant portion of the overall damping rate and can therefore not be neglected, when modeling the resonant behaviour of a cavity. The effect of intrinsic attenuation was investigated for the case of gas-filled cavity, where the effect is assumed to be largest. For realistic Q values, derived from empirical atmospheric attenuation data, it was shown that attenuation has a significant impact on the resonance peaks, especially for large frequencies. However, for low frequencies and additional HP-filtering in the spectral domain the resonance characteristics of a gas-filled cavity as modeled for the unattenuated case, could be captured from the modeling including intrinsic attenuation.

Fluid-filled cavities have much lower impedance contrasts to the surrounding medium and the damping due to energy transmission appears to be close to critical damping. In the synthetic seismograms the internal reflections are visible only for the case of the fluid-filled cavity, whereas for the gas-filled cavity, the seismograms resemble the seismograms for the vacuum case. This is explained by the low spectral width of the resonance peaks in the case of gas-filled cavities, which causes the amplitudes of the internal reflections to be very small. However, due to low damping of the internal oscillations, they may last over long time series. In case of the fluid-filled cavity, the resonance peaks are broader, due to higher damping of the oscillations and a higher transmission rate of energy from the acoustic to the elastic medium. Therefore reverberations that represent decaying acoustic reverberations become visible in synthetic seismograms.

In synthetic spatial spectrograms the acoustic resonance peaks can be identified as spectral lines whose frequencies are independent from the distance to the cavity. In that representation, resonant peaks can be identified and distinguished from long-period modulations of the primary scattered waves that shift their peak positions in the frequency domain with distance. By applying a high-pass filter to the spectrograms, the resonance peaks can be enhanced, which could lead to a possible technique to detect acoustic resonances from cavities in real experiments.

Acknowledgments

We acknowledge financial support by the Vienna Science and Technology Fund (WWTF) project MA14-006. The computational results presented in Fig. 15 have been achieved using the Vienna Scientific Cluster (VSC). We thank Lars Ceranna for sharing his expertise on intrinsic attenuation of acoustic waves in air. Two anonymous reviewers are thanked for constructive comments that improved the manuscript.

References

Adushkin, V. V., and A. A. Spivak (2004), Changes in Properties of Rock Massifs Due to Underground Nuclear Explosions, *Combustion, Explosion, and Shock Waves*, **40**(6), 624–634.

Ávila-Carrera, R., and F. J. Sánchez-Sesma (2006), Scattering and diffraction of elastic P- and S-waves by a spherical obstacle: A review of the classical solution, *Geofisica Internacional*, **45**(1), 3–21.

Budak, B. M., A. A. Samarskii, and A. N. Tikhonov (1988), *A Collection of Problems in Mathematical Physics*, 663 pp., Dover Publications, New York.

Carcione, J. M. (2014), *Wave Fields in Real Media*, 3 ed., 143 pp., Elsevier Science.

Grebenkov, D. S., and B.-T. Nguyen (2013), Geometrical Structure of Laplacian Eigenfunctions, *SIAM Review*, **55**(4), 601–667.

Gritto, R. (2003), Subsurface void detection using seismic tomographic imaging, *Lawrence Berkeley National Laboratory, Retrieved from: http://www. escholarship. org/uc/item/10b3g07v*.

Hinders, M. K. (1991), Plane-elastic-wave scattering from an elastic sphere, *Il Nuovo Cimento B Series 11*, **106**(7), 799–818.

Houser, F. N. (1970), A summary of information and ideas regarding sinks and collapse, Nevada Test Site, *Tech. rep.*, U.S. Geological Survery Report USGS-474-41 [NTS-216].

Korneev, V. (2009), Resonant seismic emission of subsurface objects, *Geophysics*, **74**(2), T47–T53.

Korneev, V. A., and L. R. Johnson (1993), Scattering of elastic waves by a spherical inclusion-I. Theory and numerical results, *Geophysical Journal International*, **115**(1), 230–250.

Korneev, V. A., and L. R. Johnson (1996), Scattering of P and S Waves by a Spherically Symmetric Inclusion, *Pageoph*, **147**(4), 675–718.

Krawczyk, C. M., U. Polom, S. Trabs, and T. Dahm (2012), Sinkholes in the city of Hamburg-New urban shear-wave reflection seismic system enables high-resolution imaging of subrosion structures, *Journal of Applied Geophysics*, **78**, 133–143.

Lambert, M., E. Saenger, B. Quintal, and S. Schmalholz (2011), Detection of a viscoelastic inclusion using spectral attributes of the quasi-stationary seismic surface response, *2011 SEG Annual Meeting*, pp. 1–4.

Sloan, S. D., S. L. Peterie, R. D. Miller, J. Ivanov, J. T. Schwenk, and J. R. McKenna (2015), Detecting clandestine tunnels using near-surface seismic techniques, *Geophysics*, **80**(5), EN127–EN135.

Sutherland, L. C., and H. E. Bass (2006), Atmospheric absorption in the atmosphere up to 160 km, *The Journal of the Acoustical Society of America*, **120**(5), 2985.

Tóth, I. T., E. B. Bujdosó, R. C. Csabafi, T. G. Gúthy, E. H. Hegedus, A. C. K. Kovács, I. T. Török, and Z. P. Prónay (2015), *Examination of a karstic cave with complex geophysical methods in North Hungary*, pp. 686–690, Near Surface Geoscience 2015 - 21st European Meeting of Environmental and Engineering Geophysics (EAGE).

List of Figures

List of Tables

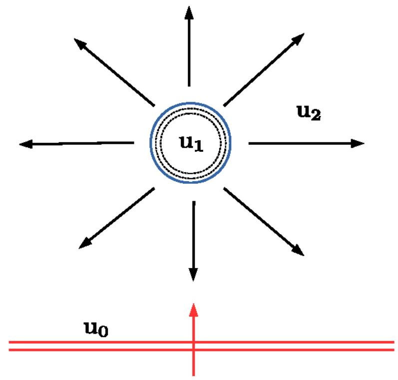

Figure 1: *Separation of seismic displacement field in incident ($\mathbf{u_0}$) and scattered ($\mathbf{u_2}$) wave-fields in the surrounding elastic medium and the acoustic wave-field inside the cavity ($\mathbf{u_1}$).*

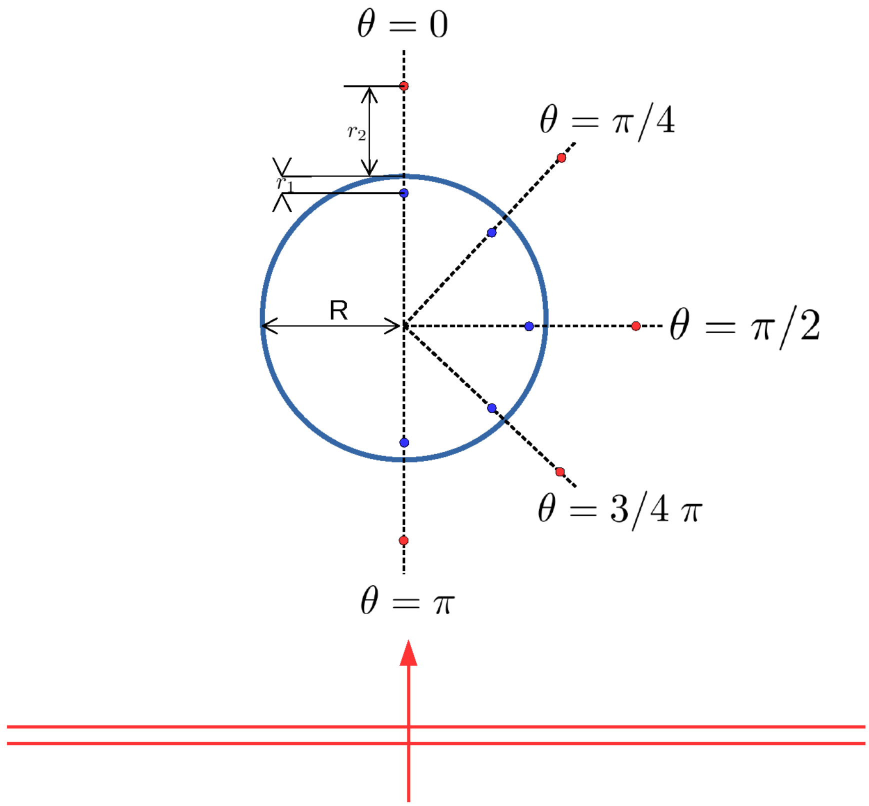

Figure 2: *Locations (monitoring points) inside and around the cavity, at which amplitude spectra are calculated and compared are marked by blue and red dots, respectively. As radius R of the cavity* 30 m, *and for the distances of the monitoring points to the cavity's interface* $r_1 = 0.1$ m *and* $r_2 = 50$ m *are chosen.*

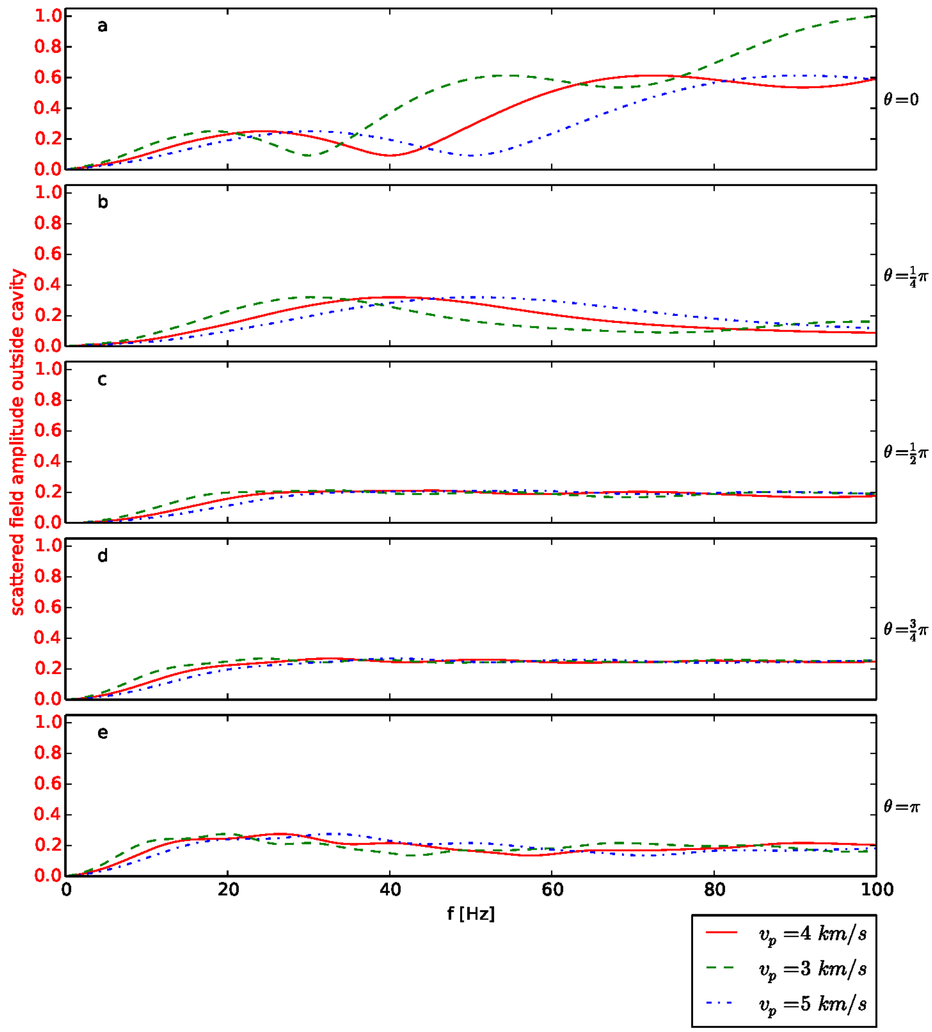

Figure 3: *Spectral amplitude variation of the scattered field in the surrounding medium for a vacuum inclusion. The variation is controlled by the velocity of the surrounding medium. Three cases are shown: v_p = 3000, 4000 and* 5000 m/s *are plotted in dashed, solid and dash-dotted lines, respectively. The ratio v_p/v_s was chosen to be* 1.73 *in all cases.*

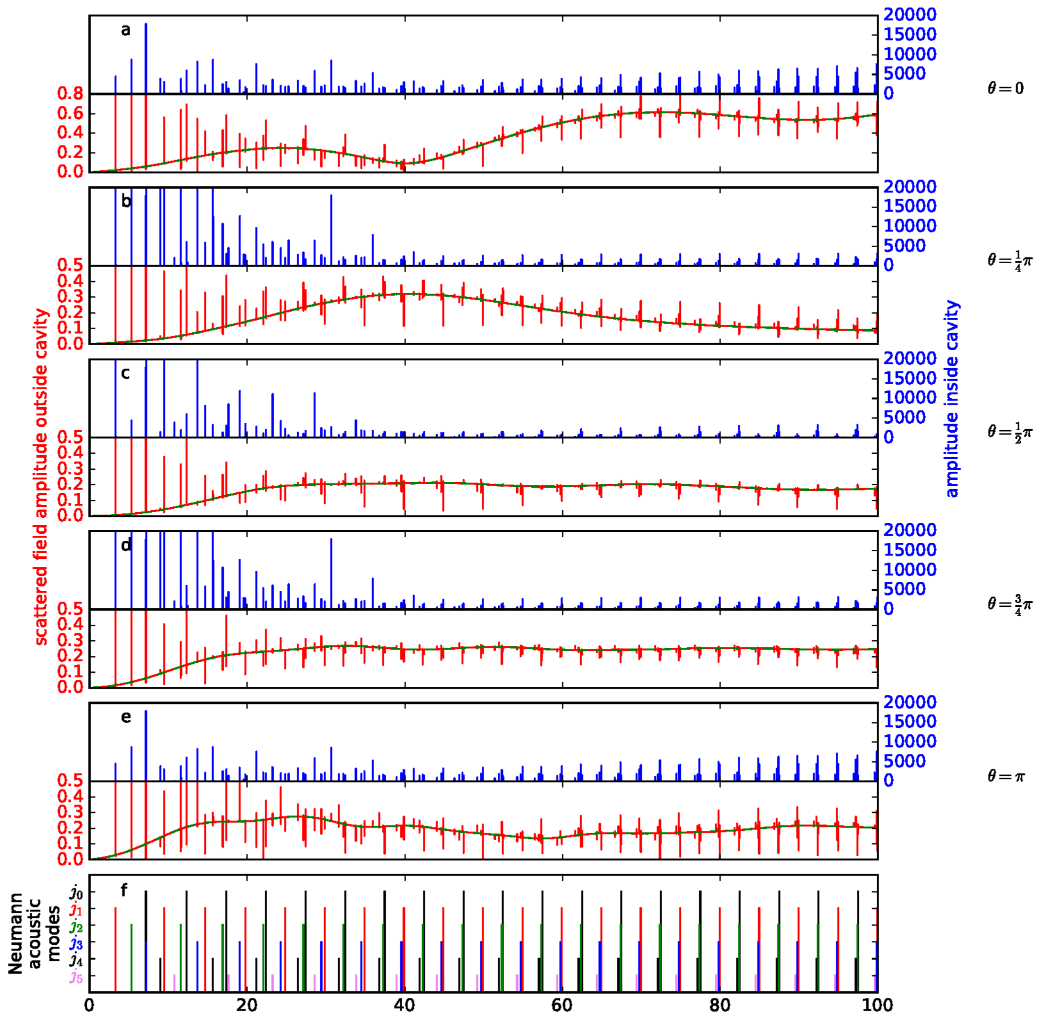

Figure 4: *Amplitude spectrum inside and outside of a gas-filled cavity for different scattering angles θ ($v_p = 4000$ m/s). The locations of points inside and outside the cavity for which the amplitude spectra are determined are shown in Fig. 2. The green dashed line shows the amplitude variation for a vacuum inclusion with the same elastic parameters as the surrounding medium. The lowest panel shows the eigenfrequencies of the gas-filled cavity with stiff boundaries (Neumann boundary condition for the pressure field) corresponding to the spherical Bessel functions, which represent the radial component of the eigenfunctions. Eigenfrequencies corresponding to the spherical Bessel functions of different orders are depicted with different lengths.*

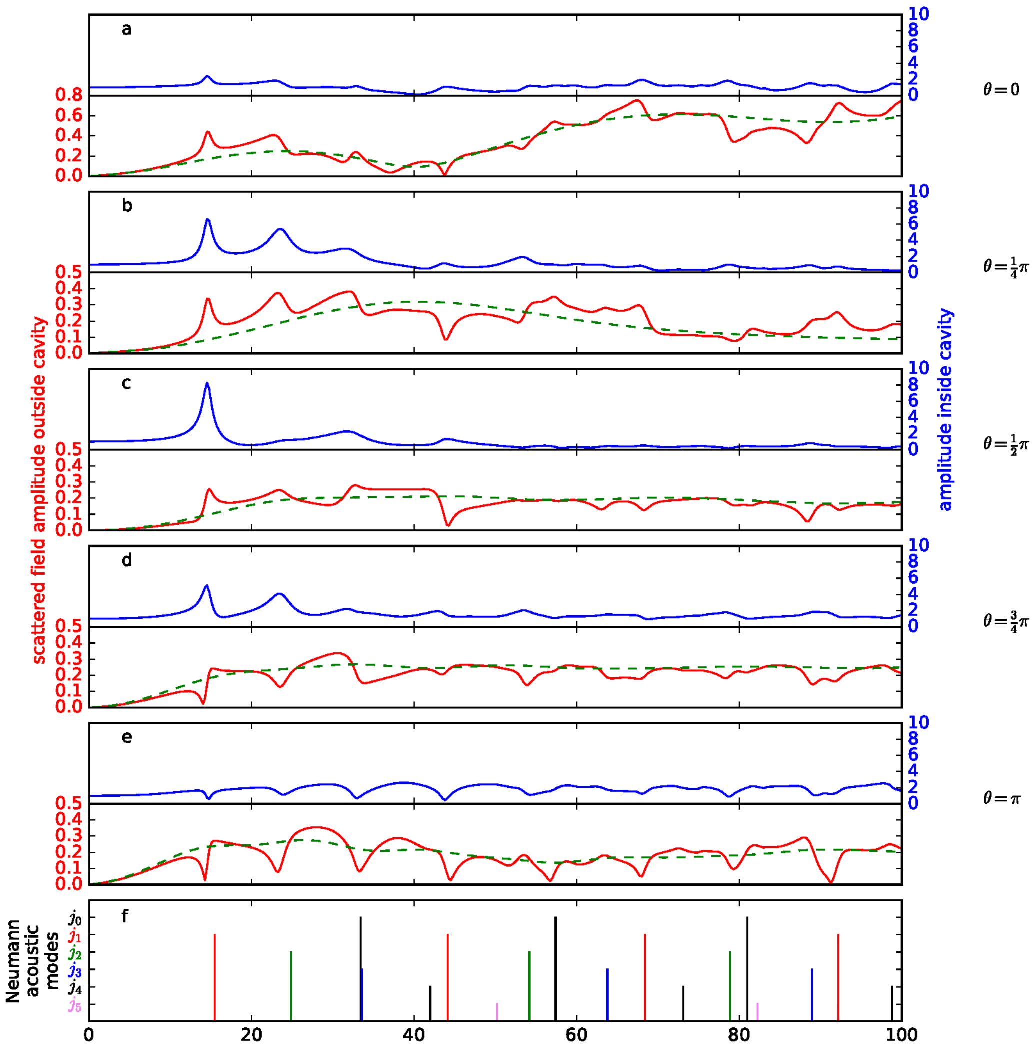

Figure 5: *Amplitude spectrum inside and outside of a fluid-filled cavity (see description of Fig. 4).*

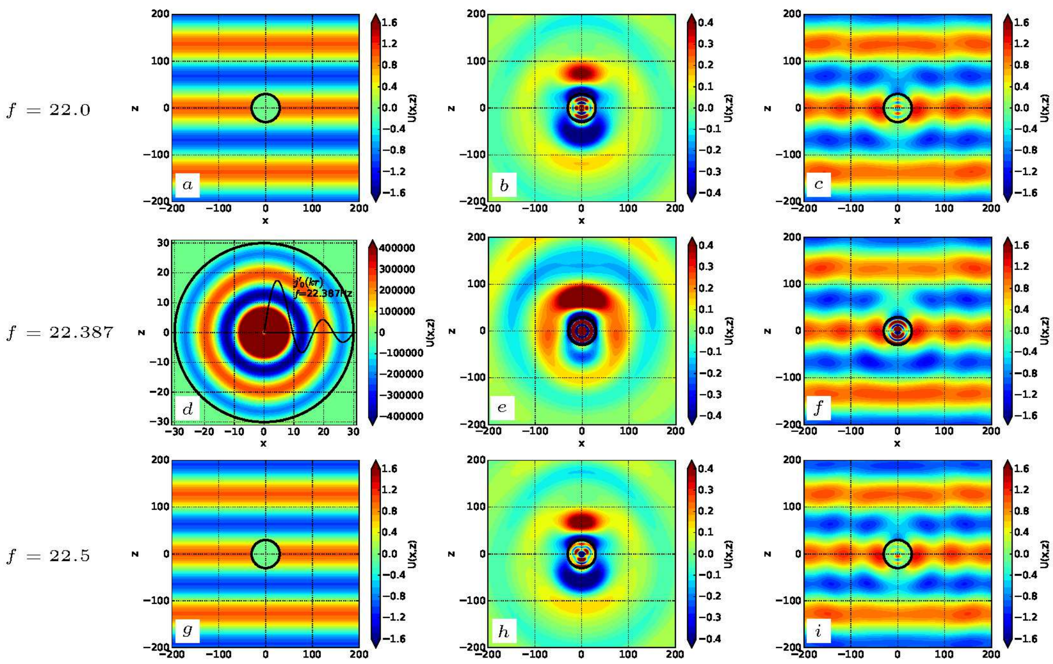

Figure 6: *Appearance of acoustic resonance for a gas-filled cavity at the Neumann eigenmode* j_{04} *(*f_{res} $=$ 22.387 Hz*). The full wave-field was derived for monochromatic incident P-waves from below. Figs. a-c were computed for* $f < f_{res}$*, Figs. d-f at the resonance frequency* $f = f_{res}$ *and Figs. g-i for* $f > f_{res}$*. The upper and lower figures in the left column (a and g) display the z-component of the incident fields for* $f < f_{res}$ *and* $f > f_{res}$*, respectively. The middle column (b,e,h) shows the radial component of the scattered fields, where the origin is located in the center of the cavity. In the right columns (c,f,i) the z-components of the corresponding total fields are shown. Fig. d shows a zoom into the cavity displaying the radial component of the scattered field for* $f = f_{res}$ *and the derivative of the spherical Bessel function j'(kr). In the surrounding elastic medium,* v_p $=$ 3.0 km/s *and* $v_p/v_s = 1.73$ *were chosen.*

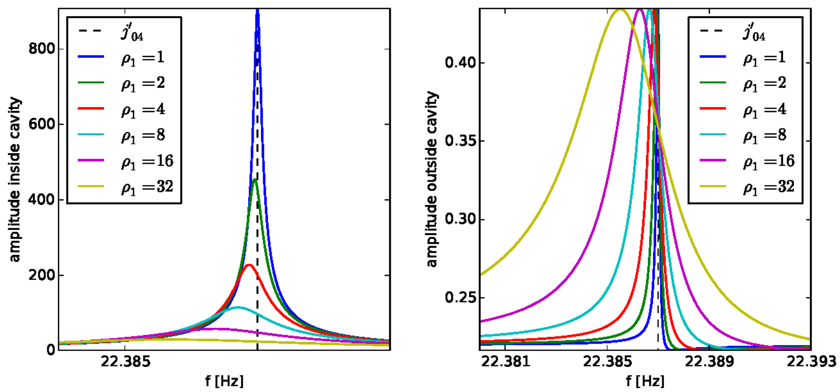

(a) *Peak inside cavity* **(b)** *Peak outside cavity*

Figure 7: *Resonant peak at Neumann eigenmode j_{04} calculated inside in the acoustic (a) and outside in the elastic (b) domain of the gas-filled cavity with different densities.*

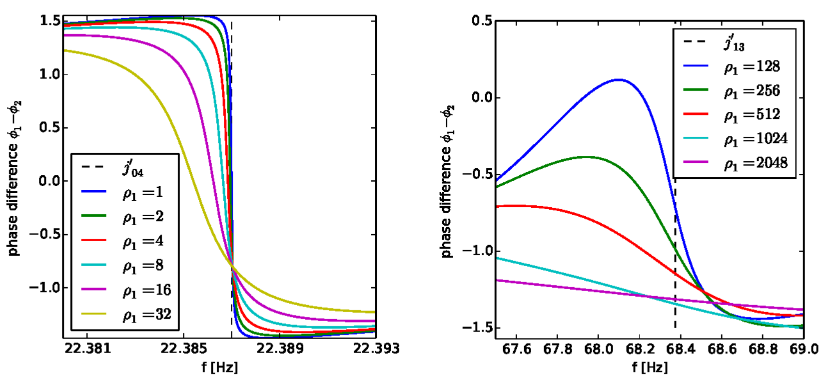

(a) *gas-filled* **(b)** *fluid-filled* a

Figure 8: *Phase difference of displacement inside and outside the cavity for varying density of the acoustic medium (as labeled). The velocity of the acoustic medium is fixed to the values of (a) a gas-filled ($v_p = 300$ m/s) and (b) a fluid-filled ($v_p = 1400$ m/s) cavity.*

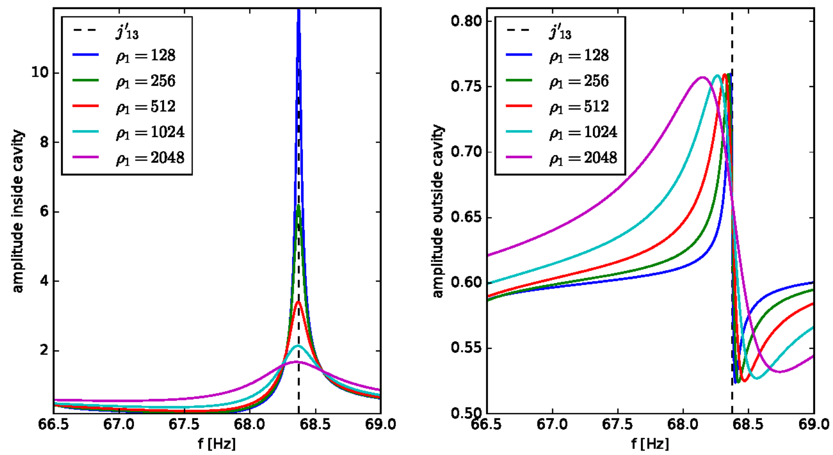

(a) *Peak inside cavity* **(b)** *Peak outside cavity*

Figure 9: *Resonance peak inside (a) vs. outside (b) the cavity at Neumann eigenmode j_{13} for a fluid-filled cavity with different densities.*

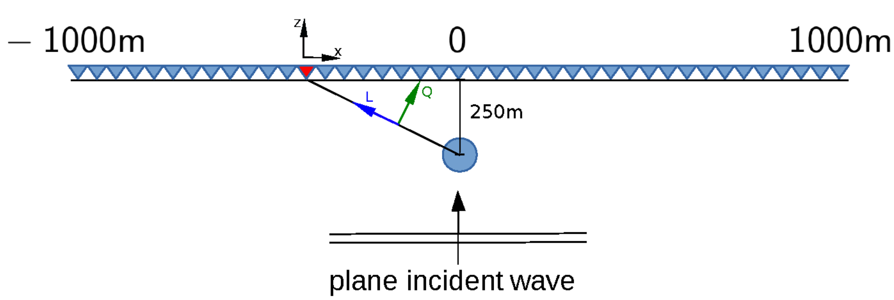

Figure 10: *Locations of receivers with respect to the cavity and the incident plane wave for the calculated synthetic seismograms. For the red marked receiver, the orientation of the L- and Q-components that are used to separate longitudinal (P) and transversal (S) displacements from the scattered wave-field are depicted.*

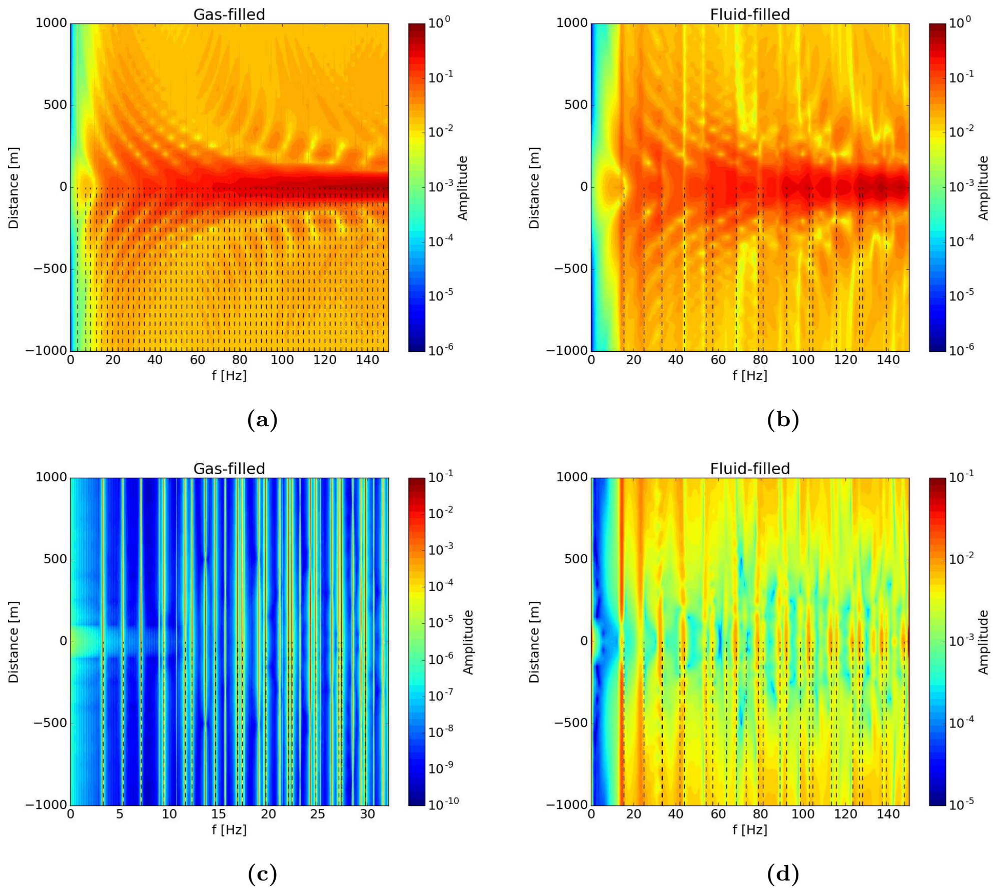

Figure 11: *Spatial spectrograms: Spatial variation of the amplitude spectrum of the scattered wave-field from the cavity for gas-filled inclusion (a,c) and fluid-filled inclusion (b,d). Dashed vertical black lines denote the positions of acoustic eigenmodes of the cavity with fixed boundaries. In c) and d) a high-pass filter was applied to the spectrum in order to suppress long amplitude variations and enhance the eigenmodes. Note that in c) the frequency range is restricted to 0 to* 32.14 Hz*, which is chosen to show the same eigenmode range in the gas-filled and fluid-filled case in c) and d).*

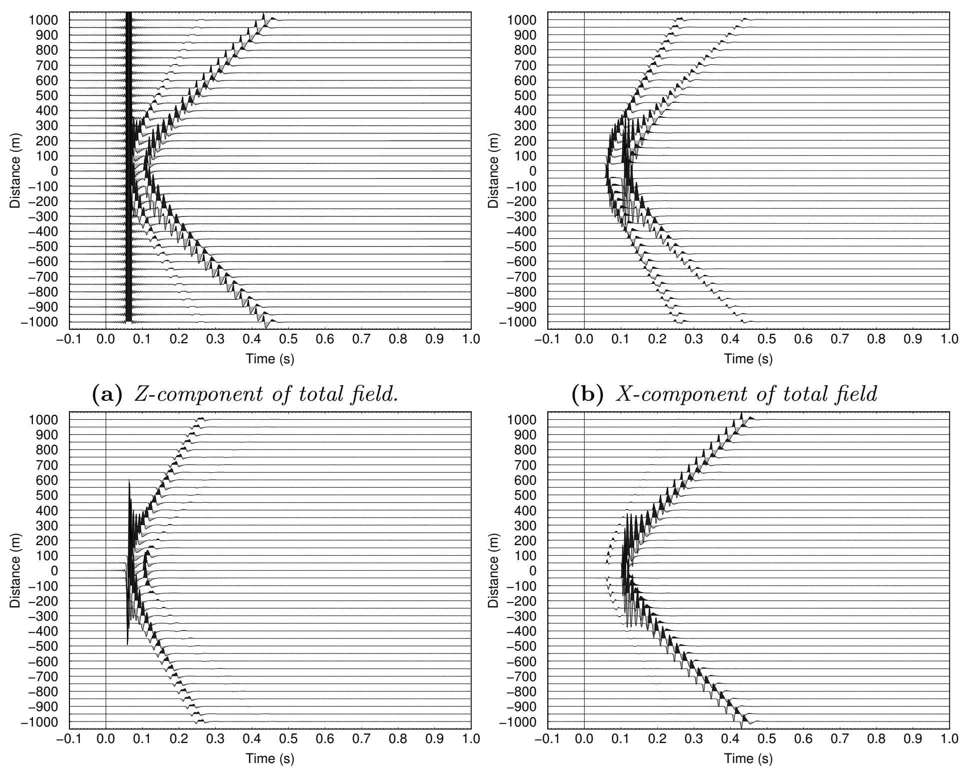

(a) *Z-component of total field.* **(b)** *X-component of total field*

(c) *L-component of scattered field* **(d)** *Q-component of scattered field*

Figure 12: *Synthetic seismograms derived from total (a-b) and scattered (c-d) field for incident plane P-wave at a gas-filled cavity. In a) and b) vertical and horizontal components of the total field are shown. c) and d) show rotated seismograms with respect to the station location and the cavities center in order to separate longitudinal and transversal particle motion.*

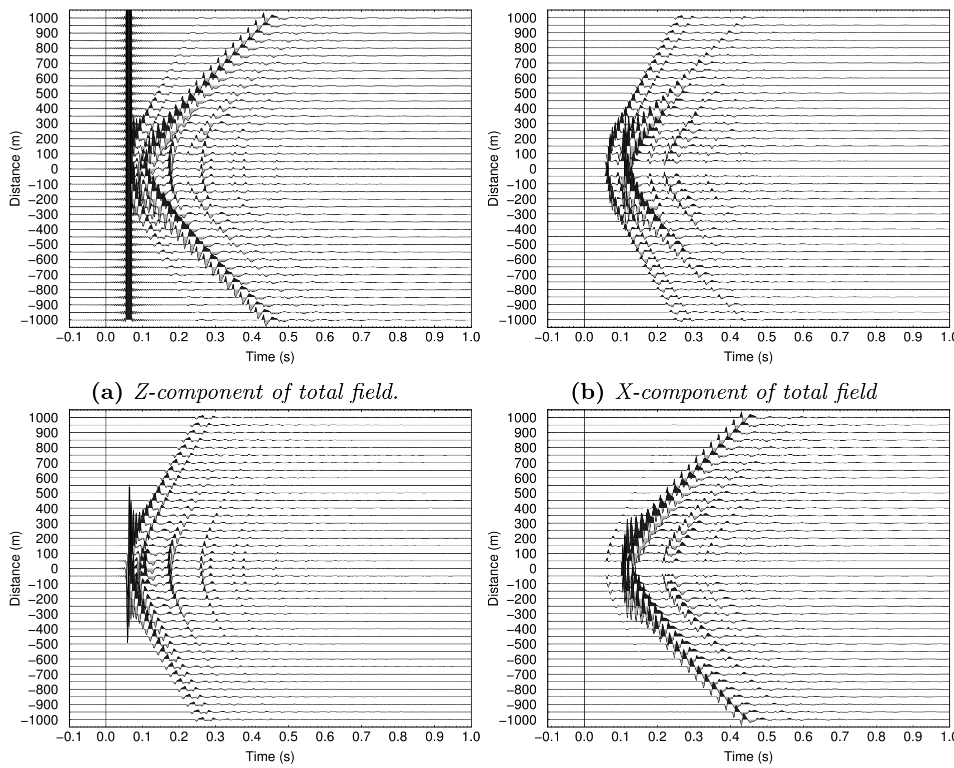

(a) *Z-component of total field.*

(b) *X-component of total field*

(c) *L-component of scattered field*

(d) *Q-component of scattered field*

Figure 13: *Synthetic seismograms derived from total (a-b) and scattered (c-d) field for incident plane P-wave at a fluid-filled cavity. In a) and b) vertical and horizontal components of the total field are shown. c) and d) show rotated seismograms with respect to the station location and the cavities center in order to separate longitudinal and transversal particle motion.*

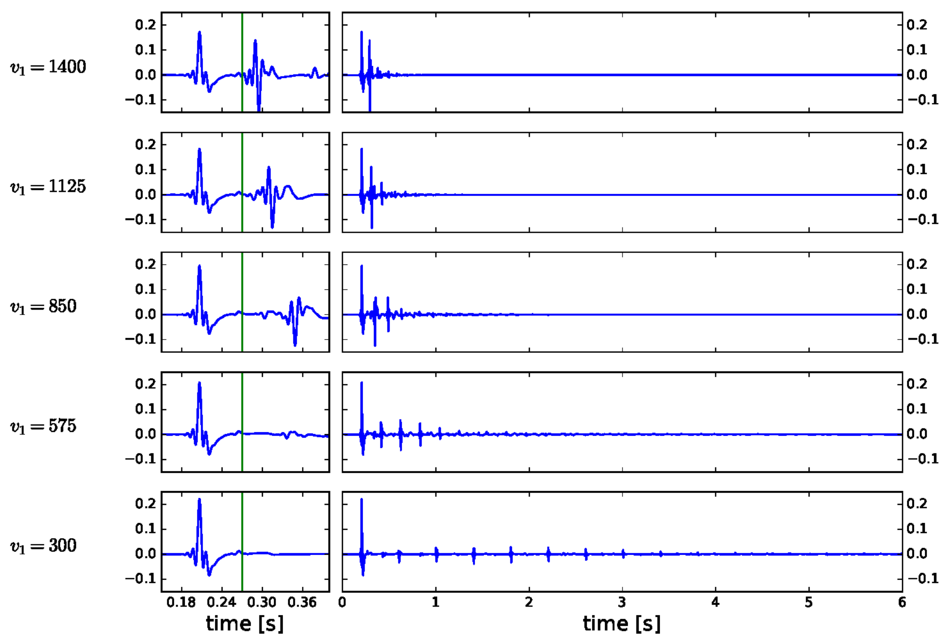

Figure 14: *Synthetic seismograms of the scattered field for different acoustic velocities (depicted on the left side of each trace) of the acoustic medium and a fixed density of* $1024\ \mathrm{kg/m^3}$. *The left column shows a zoom into the first* 0.4 s *in order to show the primary scattered pulse, which does not change for* $t < 0.27$ s *(marked by vertical green bar).*

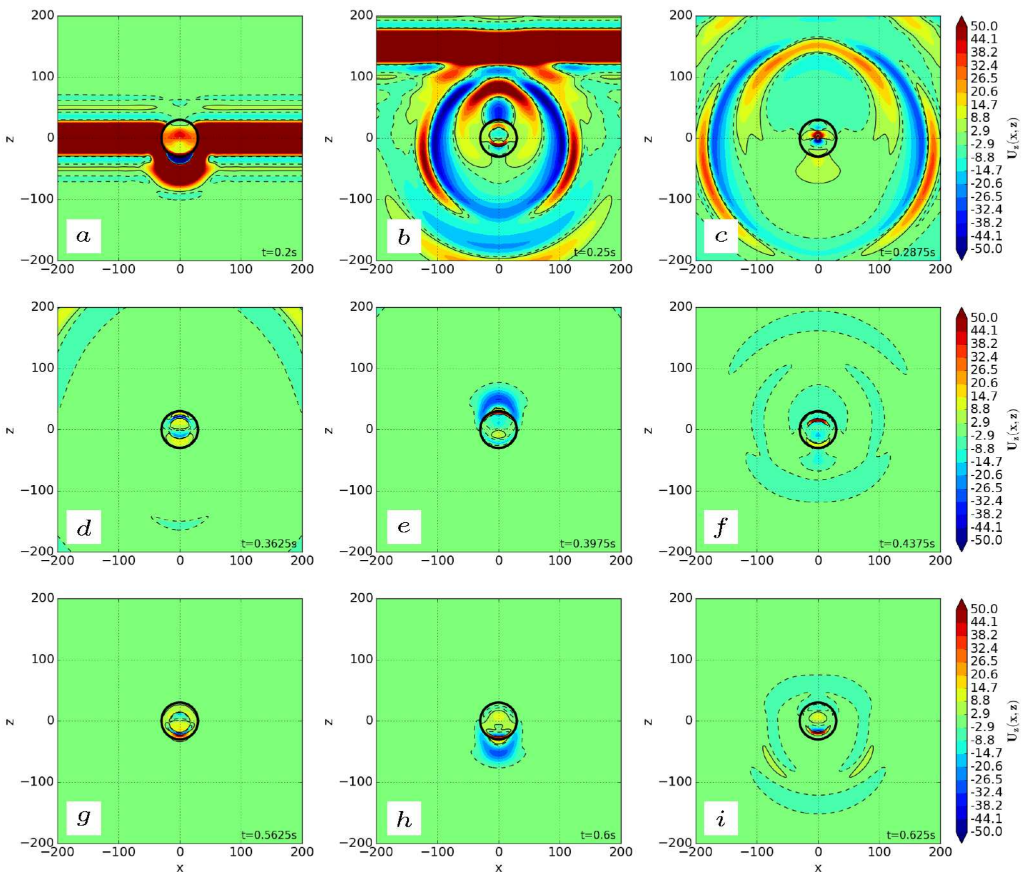

Figure 15: *Time evolution of the total wave-field for an impulsive line source, for an acoustic cavity with wave speed* $v_p = 300$ m/s *and density* $\rho = 1024$ kg/m^3. *The z-component of the displacement field is displayed color coded as snap shots for advancing time (time in* s *displayed in the lower right corner of each frame).*

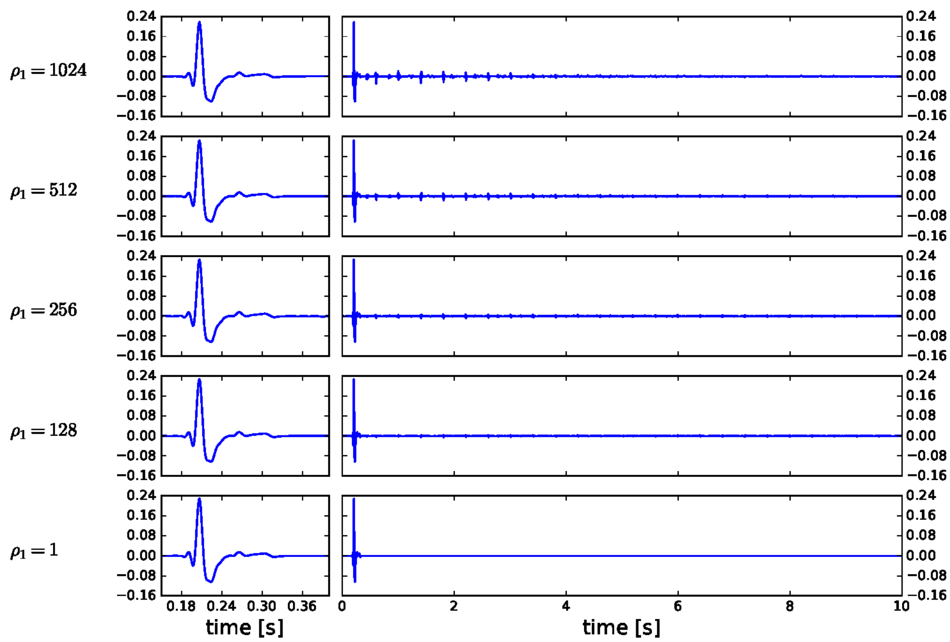

Figure 16: *Synthetic seismograms of the scattered field for different densities (depicted on the left side of each trace) of the acoustic medium and a fixed velocity of* 300 m/s. *The left column shows a zoom into the first* 0.4 s *in order to show the primary scattered pulse.*

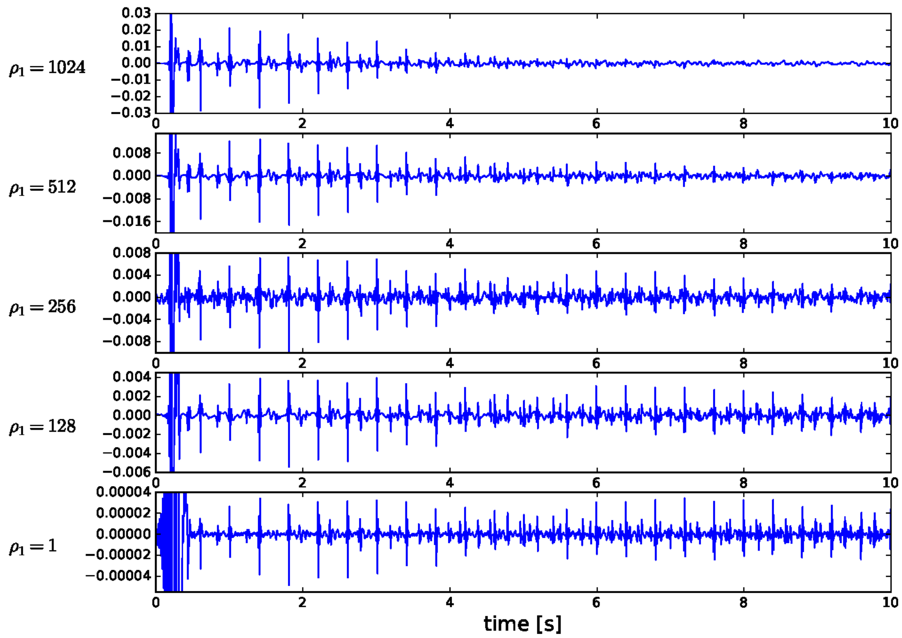

Figure 17: *Synthetic seismograms of the scattered field for different densities (depicted on the left side of each trace) of the acoustic medium and a fixed velocity of* 300 m/s. *The zoom factor of each trace is chosen in ordem to display repetitive signals from internal oscillations, achieved by increasing zoom factor from upper to lower traces as reflected by the Y-range. The zoom factor of the lowest trace is three orders of magnitude larger than the one of the top trace.*

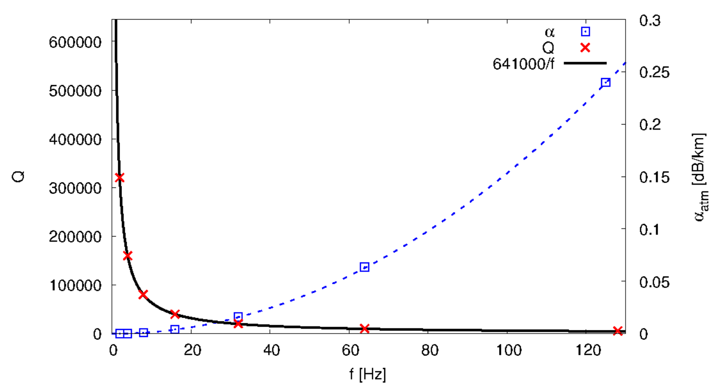

Figure 18: *Q-factor and intrinsic attenuation* α *depending on the frequency* f. *Values for* α *(blue squares) are taken from Sutherland and Bass (2006), Table IV at an altitude of* 0 km. *Values for* Q *are derived from Eq. 17. Black solid line* ($Q(f) = 641000$ Hz$/f$) *represents the least-square-fit for the empirical Q-values.*

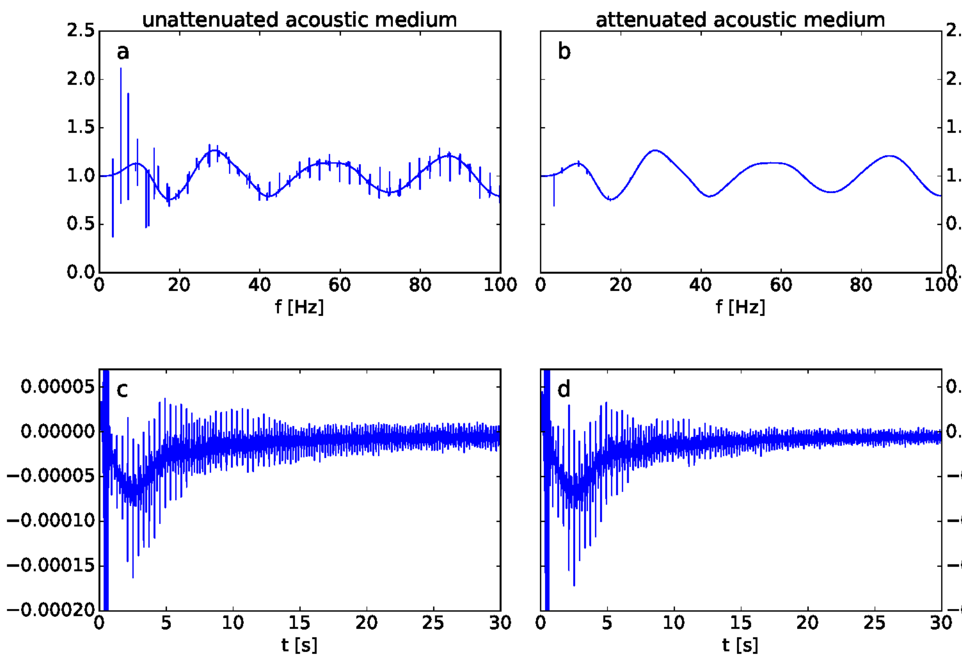

Figure 19: *Comparison of amplitude spectrum (a,b) and corresponding seismograms (c,d), calculated for the unattenuated case (a,c) and for the case of intrinsic attenuation in the acoustic medium (b,d).*

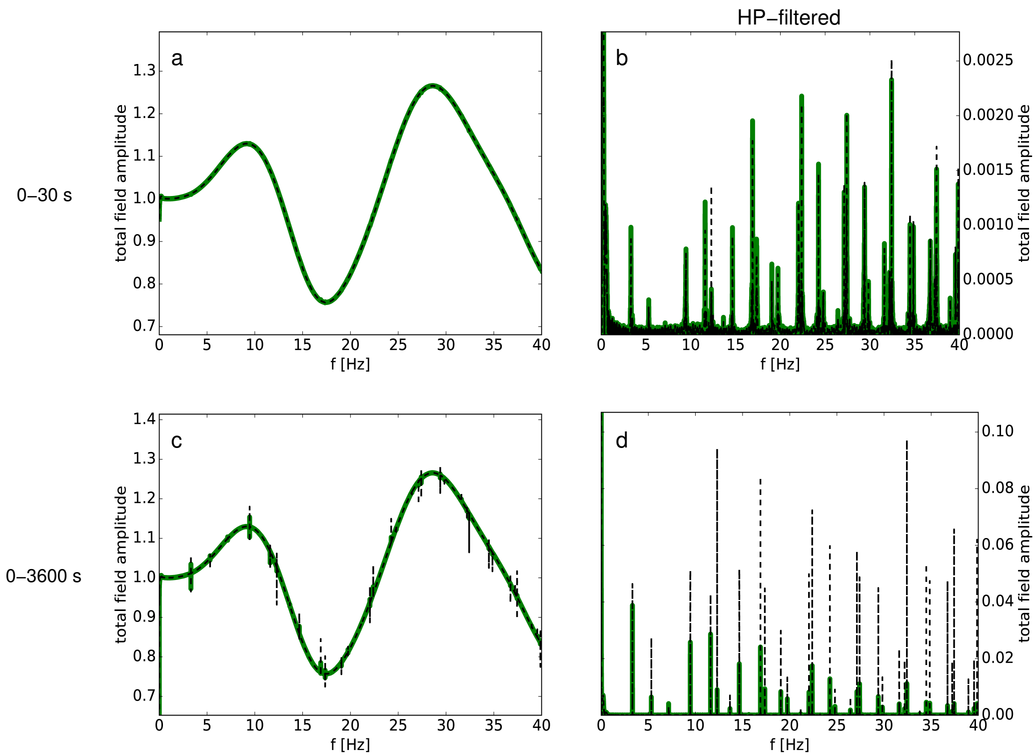

Figure 20: *Spectrum and high-pass filtered spectrum derived from synthetic seismograms taking into account* 30 s *(a,b) and 1h (c,d) of the seismogram considering intrinsic attenuation (green solid line) and for the unattenuated case (black dashed line).*

location	medium	v_p [m/s]	v_s [m/s]	ρ [kg/m^3]
inside	vacuum	0	0	0
	acoustic (gas)	300	0	1
	acoustic (fluid)	1400	0	1000
outside	elastic	4000	2312	2700

Table 1: *Choice of the acoustic and elastic parameters for the medium inside and outside the cavity, respectively.*

Appendix

The synthetic experiment discussed in section "Wave-field along seismic profile" is repeated for the back-scattering domain, i.e. the incident wave is approaching the cavity from the top, while the station profile is located 250 m above the cavity as display in Fig. A.1. Spatial spectrograms for the gas- and fluid-filled cavity are shown in Fig. A.2. The corresponding synthetic seismograms for the gas-filled and fluid-filled cavity are shown in Fig. A.3 and Fig. A.4, respectively. Qualitatively the results resemble the ones from Fig. 11, 12 and 13. The main differences in the spectrograms are the different background pattern in Fig. A.2 a and b. In the synthetic seismograms the incident wave, that is displayed in Fig. A.3 a and Fig. A.4 a at $t \approx -0.08$ s is more separated from the scattered field. Since no shadow zone appears in the back-scattering domain, the L-component of the scattered field shown in Fig. A.3 c and Fig. A.4 c is smoother compared to the transmission regime displayed in Fig. 12 c and Fig. 13 c. Note that the origin of the coordinate system is the center of the cavity that the incident wave crosses at $t = 0$.

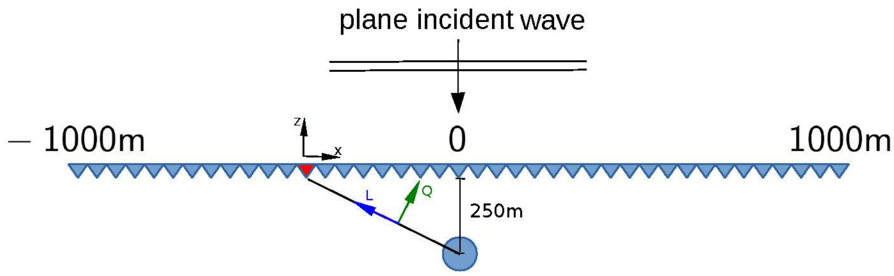

Figure A.1: *Locations of receivers with respect to the cavity and the incident plane wave for the calculated synthetic seismograms in the back-scattered regime. Description of components see Fig. 10.*

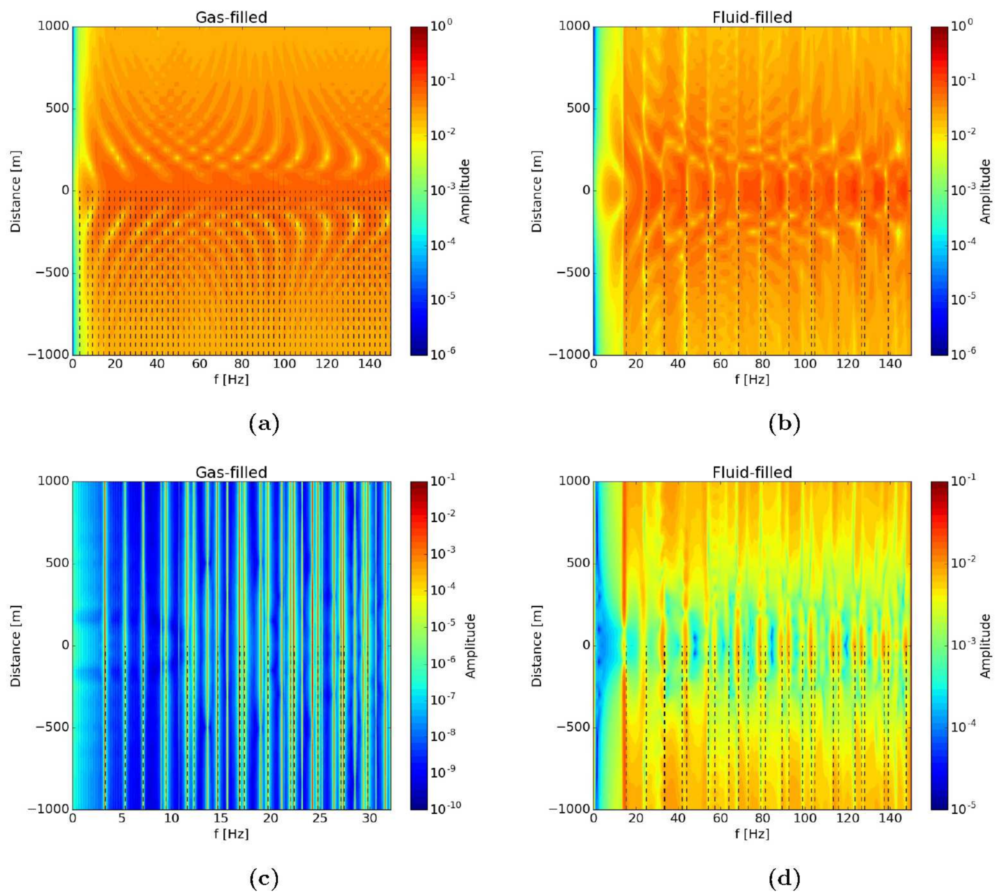

Figure A.2: *Same as Fig. 11 for the back-scattering domain.*

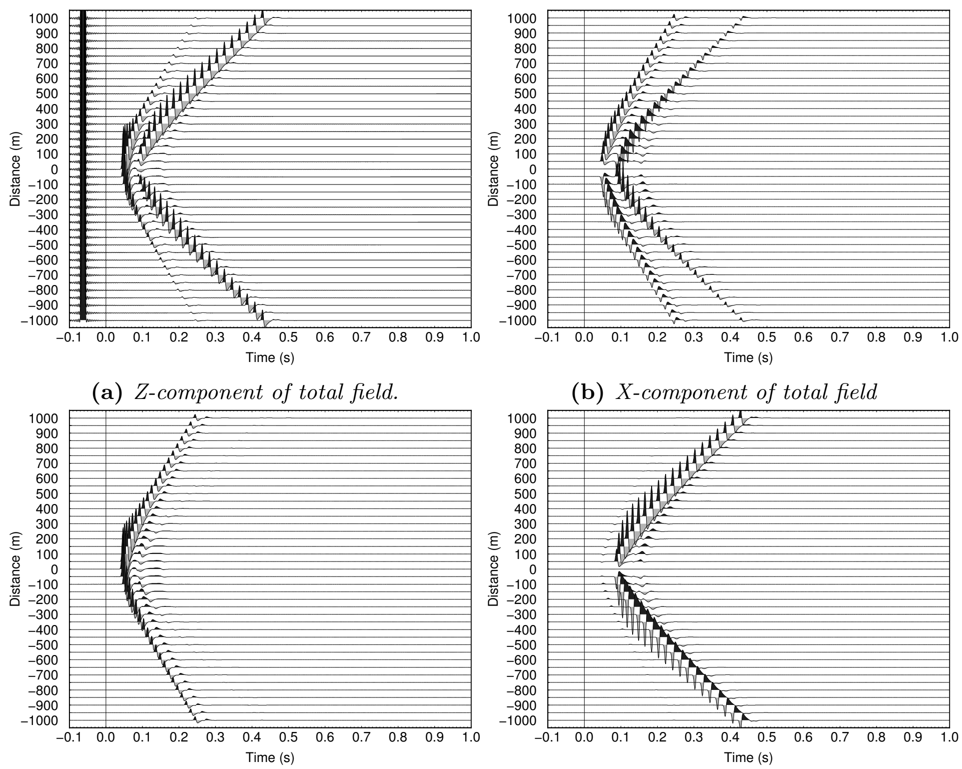

(a) *Z-component of total field.*

(b) *X-component of total field*

(c) *L-component of scattered field*

(d) *Q-component of scattered field*

Figure A.3: *Same as Fig. 12 for the back-scattering domain.*

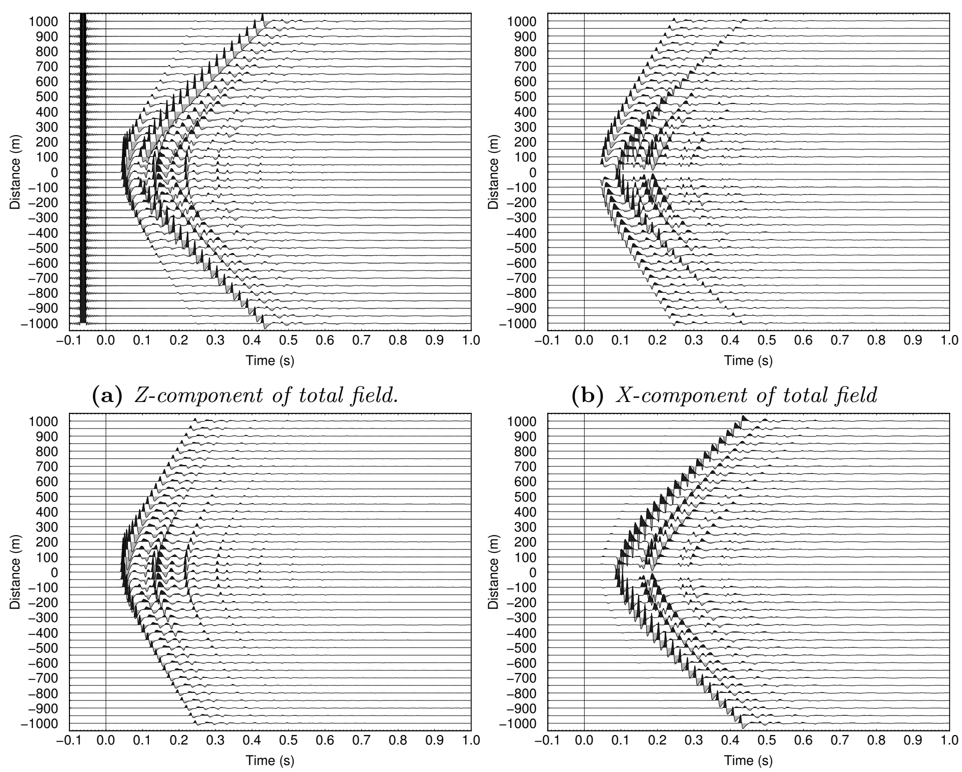

(a) *Z-component of total field.* **(b)** *X-component of total field*

(c) *L-component of scattered field* **(d)** *Q-component of scattered field*

Figure A.4: *Same as Fig. 13 for the back-scattering domain.*